The Structure of the Hydrated Electron. Part 2. A Mixed Quantum/Classical Molecular Dynamics Embedded Cluster Density Functional Theory: Single−Excitation Configuration Interaction Study

Ilya A. Shkrob,*,† William J. Glover,‡ Ross E. Larsen,‡ and Benjamin J. Schwartz*,‡

Chemistry Division, Argonne National Laboratory, 9700 South Cass Avenue, Argonne, Illinois 60439, and Department of Chemistry and Biochemistry, University of California, Los Angeles, Los Angeles, California 90095-1569

Received: December 2, 2006; In Final Form: March 5, 2007

Adiabatic mixed quantum/classical (MQC) molecular dynamics (MD) simulations were used to generate snapshots of the hydrated electron in liquid water at 300 K. Water cluster anions that include two complete solvation shells centered on the hydrated electron were extracted from the MQC MD simulations and embedded in a roughly 18 Å × 18 Å × 18 Å matrix of fractional point charges designed to represent the rest of the solvent. Density functional theory (DFT) with the Becke−Lee−Yang−Parr functional and single-excitation configuration interaction (CIS) methods were then applied to these embedded clusters. The salient feature of these hybrid DFT(CIS)/MQC MD calculations is significant transfer (∼18%) of the excess electron's charge density into the 2p orbitals of oxygen atoms in OH groups forming the solvation cavity. We used the results of these calculations to examine the structure of the singly occupied and the lower unoccupied molecular orbitals, the density of states, the absorption spectra in the visible and ultraviolet, the hyperfine coupling (hfcc) tensors, and the infrared (IR) and Raman spectra of these embedded water cluster anions. The calculated hfcc tensors were used to compute electron paramagnetic resonance (EPR) and electron spin echo envelope modulation (ESEEM) spectra for the hydrated electron that compared favorably to the experimental spectra of trapped electrons in alkaline ice. The calculated vibrational spectra of the hydrated electron are consistent with the red-shifted bending and stretching frequencies observed in resonance Raman experiments. In addition to reproducing the visible/near IR absorption spectrum, the hybrid DFT model also accounts for the hydrated electron's 190-nm absorption band in the ultraviolet. Thus, our study suggests that to explain several important experimentally observed properties of the hydrated electron, many-electron effects *must* be accounted for: one-electron models that do not allow for mixing of the excess electron density with the frontier orbitals of the first-shell solvent molecules cannot explain the observed magnetic, vibrational, and electronic properties of this species. Despite the need for multielectron effects to explain these important properties, the ensemble-averaged radial wavefunctions and energetics of the highest occupied and three lowest unoccupied orbitals of the hydrated electrons in our hybrid model are close to the s- and p-like states obtained in one-electron models. Thus, one-electron models can provide a remarkably good approximation to the multielectron picture of the hydrated electron for many applications; indeed, the two approaches appear to be complementary.

1. Introduction

This paper is the second part of a two-part series on the structure of the hydrated electron, e_{hyd}^-. Using density functional theory (DFT) and ab initio methods, in Part 1,[1] we examined several idealized water clusters that trap the electron in their interiors. Using electron paramagnetic resonance (EPR)[3−5] and electron spin echo envelope modulation (ESEEM) spectroscopies,[2,3,6] we found that octahedral anions with OH groups pointing toward the center of a spherical solvation cavity (known as Kevan's model of the hydrated electron)[2,3] account reasonably well for the observed hyperfine coupling (hfcc) tensors estimated for the electron trapped in low-temperature alkaline ices. Importantly, this result depends critically on the use of a multielectron model[1,14−16] (as opposed to the standard one-electron approach),[7−13] because the multielectron model predicts some sharing of the excess electron density between the cavity and the frontier 2p orbitals of the oxygen atoms in the OH groups forming the cavity. Without this sharing, the magnetic resonance results cannot be explained even qualitatively.[1]

Although the results from Part 1[1] are suggestive, it is not clear whether the representation of the hydrated electron by such idealized gas-phase clusters is acceptable: the hydrated electron is a dynamic entity that constantly samples configurations of water molecules that vibrate, rotate, and otherwise move around. This means that the "hydrated electron" is not a rigid structure, but a statistical average over many configurations;[7−11] in this regard, hydrated electrons are different from non-solvent-supported chemical species, so a quantitative description of the e_{hyd}^- within the multielectron approach has to address this inherent variability. Thus, the next logical step in the development of multielectron models of the e_{hyd}^- is finding a means of building this statistical picture. This is the purpose of the present study.

* To whom correspondence should be addressed. E-mail: (Shkrob) shkrob@anl.gov, (Schwartz) schwartz@chem.ucla.edu.
† Argonne National Laboratory.
‡ University of California, Los Angeles.

10.1021/jp0682816 CCC: $37.00
Published on Web 05/27/2007

One path to this goal is Car−Parrinello or Born−Oppenheimer ab initio molecular dynamics. In fact, two recent studies[17,18] of the hydrated electron used these methods. The disadvantage to these methods is their high computational demands, which limit the level of theory one can use. In the present study, we suggest a different approach that capitalizes on the historical success of one-electron models of electron solvation in rationalizing the dynamics and energetics of electron solvation.[7−13] We used adiabatic mixed quantum/classical (MQC) molecular dynamics (MD) calculations[9] to generate a dynamical trajectory of the hydrated electron in its ground electronic state, and then we extracted temporally well-separated snapshots from this trajectory. These snapshots became the input for multielectron DFT and single-excitation configuration interaction (CIS) calculations. In these calculations, we explicitly considered only one or two complete solvation shells for the excess electron; the remaining atoms were replaced by point charges, a procedure we refer to as matrix embedding. A few hundred such snapshots are sufficient to build a robust picture of the excess electron in water.

We find that there is significant sharing of spin and charge of the excess electron by O 2p orbitals in the first-shell water molecules (a result which was hinted at in both Part 1[1] and other studies).[14−16] The ground state of the "hydrated electron" appears to be an unusual kind of multimer radical anion[3] in which ∼20% of the excess electron is shared among several first-shell water molecules and ∼80% of the electron occupies a cavity between molecules. We also find that the sharing of electron density with the first-shell solvent molecules is consistent with most of the known experimental properties of the e_{hyd}^- and is, in fact, necessary to account for some of these properties.[19−21] Although the true multielectron picture of the e_{hyd}^- is complex, on average, the radial density for the highest occupied (HOMO) and the three lowest unoccupied (LUMO) molecular orbitals resemble the s-like and p-like orbitals predicted by the one-electron models.[8b,9,11] For some observables (e.g., the optical spectrum in the visible), the fine details of this orbital structure do not matter; for other observables (e.g., the spin density maps provided by EPR and ESEEM spectroscopies and the resonance Raman spectrum), a single-electron approximation is inadequate.

The rest of this paper is organized as follows: The computational details are given in Section 2. In Section 3.1, we use a DFT method to examine the structure of the singly occupied molecular orbital. In Section 3.2, we analyze the density of states and the lower unoccupied molecular orbitals and use the CIS method to calculate the absorption spectrum. In Section 3.3, we use the calculated electronic structure to simulate matrix EPR and ^{2}H ESEEM spectra of the e_{hyd}^-. In Section 3.4, we discuss the vibrational properties. Finally, these results are summarized in Section 4. In order to reduce the length of this paper, some material (figures with the designator "S" (e.g., Figure 1S) and Sections S1−S4) is placed in the Supporting Information.

2. Computational Details

The details of MQC MD calculations[9,22−25] for a 200 water molecule supercell are given in Section S1 in the Supporting Information. A sequence of 1000 snapshots separated by a time interval of $\Delta t = 100$ fs was extracted from the trajectory. In each of the extracted snapshots, the coordinates were shifted so that the center of mass of the electron, *X*, was at the origin and minimum image periodic boundary conditions were applied. Water molecules were treated explicitly if the distance r_{XH} between *X* and one of the protons, H, was less than a chosen cutoff radius, r_{cut}; the cluster size, *n*, is then defined as the number of such water molecules. The remaining "matrix" molecules were replaced[26,27] by point charges (chosen to be the same as in the flexible simple-point charge (SPCf) model),[23] $Q_H = +0.41$ for hydrogen and $Q_O = -2Q_H$ for oxygen (in the following, such water anion and neutral clusters are referred to as "embedded" ones). With the exception of the IR-Raman simulations, the cutoff radius r_{cut} was chosen to be 4.75 Å, which corresponds to the first two solvation shells around the electron cavity; for the IR-Raman calculations, r_{cut} was set to 3 Å. We define the first solvation shell as including those water molecules for which at least one of the protons has $r_{XH} < 3$ Å. We then label the protons satisfying this condition by H_{in} ("inside"), and the protons *in the first solvation shell* that do not satisfy this condition, by H_{out} ("outside"). We also label oxygen atoms in the first solvation shell "inside" and those in the second solvation shell, "outside." The coordination number of the electron, n_H, is defined as the number of H_{in} protons. Histograms of the quantities n_H and *n* are shown in diagrams i and ii of Figure 1a, respectively. The cavity electron is coordinated by 3−8 hydroxyl groups (with a mean coordination number $\langle n_H \rangle$ of ∼6) inside a cluster of 12−25 water molecules (with an $\langle n \rangle$ of ∼20 molecules). Figure 2 displays the *X*−H and *X*−O histograms for "inside" and "outside" atoms, as defined above, and Table 1 summarizes the mean values of the *X*−H_{in} and *X*−H_{out} distances, which are 2.4 Å and 3.4 Å, respectively. The mean *X*−H_{in} distance from these one-electron snapshots is considerably longer than the 2.1−2.2 Å distance suggested by magnetic resonance experiments on alkaline ices.[2,4,6]

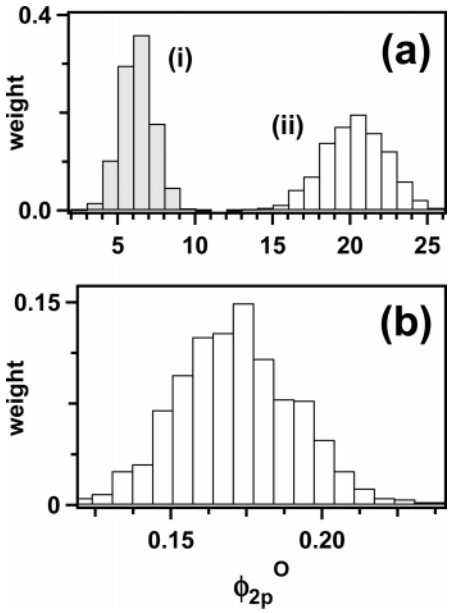

Figure 1. (a) Histograms of (i) the coordination number n_H and (ii) the cluster size *n* for the e_{hyd}^-, $r_{cut} = 4.75$ Å (the average of 1000 snapshots along the 100 ps of the MQC MD trajectory; B3LYP/6-311++G** model) and (b) the histogram for the population of O 2p orbitals, ϕ_{2p}^O, as defined in Section 3.1.

The electronic structure of the embedded water cluster anion snapshots was first modeled using unrestricted DFT with the B3LYP functional (Becke's exchange functional[28] and the correlation functional of Lee, Yang, and Parr)[29] from Gaussian 98 and 03.[30] The justification for using this implementation of DFT as opposed to ab initio molecular orbital methods for calculating magnetic resonance information was provided in Part 1 of this study.[1] The main attraction of this particular compu-

TABLE 1: Calculated Parameters for the e_{hyd}^- [a]

parameter	average[b]	parameter	average[b]
M_2^H, G^2	17.3 ± 4.6	$\langle r_{XH}\rangle_{in}$, Å	2.43 ± 0.12
iso	3.9 ± 3.1	$\langle r_{XO}\rangle_{in}$, Å	3.42 ± 0.11
aniso	13.4 ± 3.4	$\langle a^H\rangle_{out}$, G	0.09 ± 0.06
M_2^O, G^2	6050 ± 140	$\langle B_{zz}^H\rangle_{out}$, G	0.64 ± 0.05
iso	6000 ± 140	$\langle B_{zz}^O\rangle_{out}$G	-0.3 ± 0.5
aniso	52 ± 14	$\langle \rho_s^H\rangle_{out}$, $\times 10^3$	7.7 ± 2.8
$\langle a^H\rangle_{in}$, G	0.38 ± 0.50[c]	$\langle \rho_s^O\rangle_{out}$, $\times 10^3$	-0.33 ± 2.00
$\langle a^O\rangle_{in}$, G	-15.2 ± 2.2	$\langle \rho_c^H\rangle_{out}$	0.34 ± 0.01
$\langle B_{zz}^H\rangle_{in}$, G	3.7 ± 0.5	$\langle \rho_c^O\rangle_{out}$	-0.69 ± 0.02
$\langle B_{zz}^O\rangle_{in}$, G	-2.5 ± 0.7	$\langle r_{XH}\rangle_{out}$	4.44 ± 0.10
$\langle \rho_s^H\rangle_{in}$	0.10 ± 0.03	$\langle r_{XO}\rangle_{out}$	4.79 ± 0.10
$\langle \rho_s^O\rangle_{in}$	-0.042 ± 0.010	ϕ_{2p}^O	0.17 ± 0.02
$\langle \rho_c^H\rangle_{in}$	0.11 ± 0.05	$\langle n\rangle$	19.7 ± 2.0
$\langle \rho_c^O\rangle_{in}$	-0.56 ± 0.03	$\langle n_H\rangle$	5.7 ± 1.0
$\langle r_g\rangle$, Å	2.74	E, eV[d]	-1.69 ± 0.36

[a] Matrix-embedded water cluster anions with $r_{cut} = 4.75$ Å. [b] Standard deviations are given next to the mean values. [b] The most probable value is -0.4 ± 0.1 G. [c] Orbital energy of HOMO.

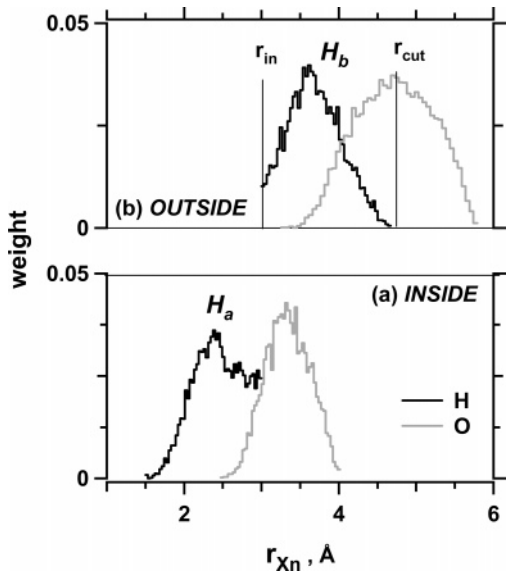

Figure 2. The histogram of distances r_{Xn} to H and O nuclei, from the center of mass of the electron X as defined in the MQC MD model, for $r_{cut} = 4.75$ Å clusters. The nuclei are divided into two groups: "inside" and "outside," as explained in Section 2.2. Black curves are for hydrogens, gray curves are for oxygens. The mean r_{XH} distance for H_{in} hydrogens is 2.4 Å (see Table 1 for other mean values). The positions of r_{in} and r_{cut} radii are indicated by vertical lines.

tational method is that it is known to accurately reproduce hfcc tensor parameters.[31] As noted in Part 1,[1] the structure of the HOMO and the lower three unoccupied Kohn−Sham (KS) orbitals obtained using B3LYP method are qualitatively similar to those obtained using Hartree−Fock (HF) and Moller−Plesset methods (MP2) for the same basis set and cluster geometry. In particular, substantial transfer of the spin density into the frontier O 2p orbitals is observed in these ab initio calculations, as well (see Section 3.2).

Unless otherwise specified, for all of our DFT calculations, a 6-31G split-valence, double-ζ Gaussian basis set augmented with diffuse and polarized (d, p) functions (6-311++G**) was used,[30] with a ghost "Cl atom" placed at the electron's center of mass, X (that is, a suite of floating orbitals and a DFT quadrature grid corresponding to a chlorine atom). These calculations yielded *isotropic* hfcc's $a^{H,O}$ for the ^{1}H nuclei (the hfcc's on deuterons are 6.5 times smaller) and ^{17}O nuclei, defined as[32]

$$a = (8\pi/3) g_e \beta_e g_n \beta_n \rho(0) \quad (1)$$

where g_e and g_n are the electron and the nuclear g-factors, and β_e and β_n are the corresponding magnetons, and $\rho(0)$ is the spin density on the nucleus, and also provided the *anisotropic* hyperfine coupling tensors **B** (that is, the electron−nucleus magnetic dipole interaction) defined through[32]

$$\mathbf{B}_{ik} = g_e \beta_e g_n \beta_N \langle r^{-5}(3 r_i r_k - r^2 \delta_{ik})\rangle \quad (2)$$

where r_i is the Cartesian component of the radius vector **r** pointing from the nucleus to the electron, and $\langle\ \rangle$ stands for averaging over the unpaired electron density. These traceless hyperfine tensors, with principal values of (B_{xx}, B_{yy}, B_{zz}), were nearly axial, so that $B_{xx} \approx B_{yy} = T_\perp$ and $B_{zz} = -2T_\perp$[6] (observe that for ^{1}H and ^{2}H, $B_{zz}^H > 0$, whereas for ^{17}O, $B_{zz}^O < 0$ because the nuclear moment for ^{17}O is negative). Below, the hfcc's are given in units of Gauss (1 $G = 10^{-4}$ T); to convert these constants to frequency units (MHz), they should be multiplied by 2.8. These hfcc data also were used to calculate (using the method detailed in Appendix B in ref 1) (i) the second moments ($M_2^{O,H}$) of the EPR spectra from the ^{1}H and ^{17}O nuclei, respectively, (eq B7 therein), (ii) the EPR spectra themselves (eq B3 therein), and (iii) ESEEM spectra (eqs B12−B16 therein). We also used Mulliken population analysis to determine the atomic spin ($\rho_s^{H,O}$) and charge ($\rho_c^{H,O}$) density on the corresponding atoms; all of the calculated parameters from our hybrid DFT/MQC MD model calculations are given in Table 1.

The IR and Raman spectra of embedded clusters and individual water molecules were calculated using the DFT/6-31+G** method.[30] It is important to note that since the water molecules in the embedded clusters are not at their stationary points, the frequencies calculated from diagonalization of the Hessian matrix correspond to making a local harmonic, or instantaneous normal mode, approximation. Although our use of such an approximation decreases the fidelity of our vibrational analysis, we know of no obvious way in which this shortcoming of our hybrid model can be overcome. Thus, although we do not expect our model to produce quantitatively accurate vibrational spectra, insight can be gained from observing how our calculated vibrational spectra's features change with and without the presence of the excess electron. Once we completed the locally harmonic analysis, the resulting "line" spectra (for normal modes only) were binned (with the bin width set to 50 cm^{-1}) to produce the spectra shown in Section 3.4. These line spectra were used to calculate centroids $\langle\nu\rangle$ of a given band (ν_{min} ,ν_{max}) (see Table 2) defined as

$$\langle\nu\rangle = \int_{\nu_{min}}^{\nu_{max}} d\nu\ \nu\ I(\nu) / \int_{\nu_{min}}^{\nu_{max}} d\nu\ I(\nu) \quad (3)$$

where $I(\nu)$ is the calculated intensity. Although our ensemble of snapshots is too small to obtain high-quality IR-Raman spectra, it was sufficient to locate the band centroids within the accuracy of several cm^{-1}, as we found by comparing the centroids calculated using eq 3 with centroids from smaller subensembles.

For simulation of electronic spectra, we performed CIS calculations of the occupied and first 10 excited states, denoted as CIS ($N = 10$), generating both transition dipole moments and transition energies for the absorption spectrum of the e_{hyd}^-. Due to the computational demands of CIS, a reduced 6-31+G* basis set was used, including a ghost "Cl" atom at the electron's center of mass. It was found that using this smaller basis did not greatly affect the excitation energies or transition dipoles.

TABLE 2: Centroids for Vibrational Bands Shown in Figures 11 and 12

band	type	*a*	*b*	*c*	*d*
libration 450−1400 cm^{-1}	IR	828.5	925.4	949.6	−
	Raman	789.4	789.4	941.5	−
H−O−H bend 1500−2000 cm^{-1}	IR	1697.8	1732.7	1755	1747.4
	Raman	1697.5	1677.3	1771.5	1754.1
H−O stretch 2200−4100 cm^{-1}	IR	2938.8	3018	2993.1	3127.8
	Raman	2952.8	2966.3	3029.4	3118.4

[a] e_{hyd}^- (embedded water anion cluster for r_{cut}=3 Å). [b] The same geometry as in part a, for a neutral cluster containing a point charge at *X*. [c] For embedded neutral water cluster with $r_{cut} = 3.5$ Å. [d] Embedded individual water molecules. In these calculations, the clusters/molecules were embedded in a matrix of point charges with $Q_H = +0.41$.

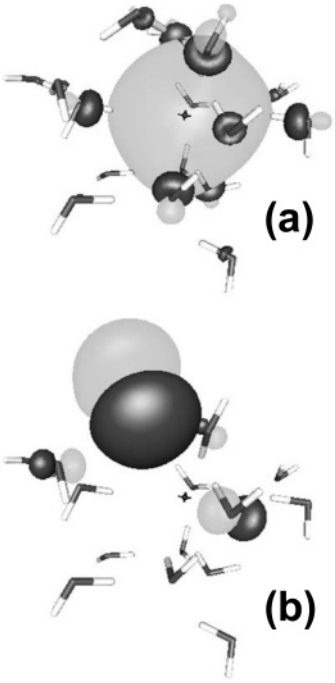

Figure 3. Isovalue surfaces of (a) the (HOMO) and (b) the (HOMO-1) calculated for a typical embedded water anion cluster using our DFT/MQC MD method (isovalue $\pm$ 0.025a_0^{-3}). Two more such SOMO maps, for three different isovalues, are shown in Figure 2S. The cross at the cavity center indicates the center of mass *X* of the electron in the MQC MD model. Light shade is for positive and dark shade is for negative parts of the wavefunction.

Oscillator strengths were calculated by averaging the line spectrum from each configuration over the ensemble of snapshots as well as binning the transitions in frequency space.

3. Results

3.1. The "s-Like" Ground State. An important part of our DFT analysis was the examination of the orbital structure and, in particular, the singly occupied molecular orbital (SOMO), Ψ, which is also the HOMO. In one-electron models, the wavefunction of the "s-like" ground state of the e_{hyd}^- is contained almost entirely within the solvation cavity.[8−12] In our model, however, we observe that the SOMO is shared between the cavity and the O 2p orbitals of the first-shell water molecules. A typical isodensity surface map of the SOMO is shown in Figure 3a. Examination of Figure 3a (and the model clusters examined in ref 1) indicates that in addition to the cavity, part of the SOMO occupies the frontal lobes of 2p orbitals of

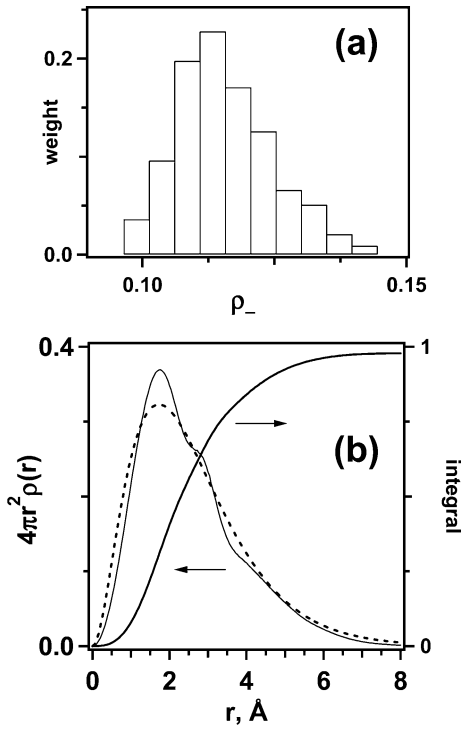

Figure 4. (a) Histogram of the integrated negative density, ρ_-, defined in eq 4. The average is 0.12. (b) The solid curve plotted to the left is the angle-averaged SOMO density $4\pi r^2\rho(r)$ given by eq 5 (the solid curve to the right is the integral of this radial density, which approaches unity for $r \rightarrow \infty$). The dashed curve is a least-squares fit to this radial density using eq 6, for $\lambda \approx 1.67$ Å. The most probable position of the electron is at $r = 1.75$ Å. The features observed between 2.5 and 3.5 Å are from O 2p orbitals.

the oxygen atoms in the first solvation shell. Because the wavefunction inside the cavity and in these frontal lobes have opposite signs, in the following, we choose a phase convention so that the intracavity SOMO is positive. In this regard, the SOMO shown in Figure 3a is consistent with previous ab initio molecular orbital and DFT calculations for gas-phase water anions that internally trap an electron.[1,15,16]

Using the fact that most of the SOMO density on the water molecules is contained in the frontal lobes of O 2p orbital and has phase opposite to the SOMO density in the cavity, we found it useful to define "positive" and "negative" charge densities via

$$\rho_\pm = \int d^3\mathbf{r}\, \Psi(\mathbf{r})^2\, \theta(\pm\Psi) \qquad (4)$$

where $\theta(\,)$ is the Heaviside step (the phase is chosen so that $\rho_+ > \rho_-$). Figure 4a shows the histogram of ρ_-: the negative part accounts for 10−14% of the total SOMO density with an expectation value of 12% (there is additional electron density in positive lobes of the O 2p functions). Consistent with the conventional way in which the spin density in the p orbitals is determined from experimental EPR data,[1,32] we estimated the total spin density, ϕ_{2p}^O, in the O 2p orbitals of (several) water molecules from the sum $\sum_O B_{zz}^O/B_{zz}^O$(at.) taken over all ^{17}O nuclei, where B_{zz}^O(at.) ≈ -104 G is the corresponding atomic constant (see also Part 1).[32] The advantage of quantifying the orbital overlap this way (as compared to, e.g., orbital decomposition into atomic wavefunctions) is that the tensor given by eq 2 "filters out" the components of the correct symmetry and thus provides a local measure of the p character. This calculation indicates an 18 $\pm$ 2% total overlap of the SOMO with the O 2p orbitals (see Figure 1b for the histogram of this quantity).

Thus, the penetration of the hydrated electron's wavefunction into the water molecules of the first solvation shell is not negligible.

To better characterize the SOMO, we found it convenient to introduce the angle-averaged (radial) density $\rho(r)$ of the electron wavefunction, defined through equation

$$4\pi r^2\rho(r) = \langle \int \mathrm{d}\Omega r^2\Psi^2(\mathbf{r})\rangle \tag{5}$$

where Ω represents the solid angle, and the angled brackets indicate an average over the ensemble of snapshots. We plot the quantity $4\pi r^2\rho(r)$ and its running integral over r in Figure 4b, which shows that the most probable position of the excess electron is $r \approx 1.75$ Å, well inside the cavity, given that the most probable $X-H_{in}$ distance is 2.26 Å. Figure 4b also shows that 50−60% of the spin density is contained within a 2.2−2.4 Å sphere and that 75% is contained within the 3 Å cutoff radius that we used to define the first shell of water molecules. The figure also shows the diffuseness of the excess electron's wavefunction: ∼5% of the spin density is contained beyond the most probable location of the H_{out} protons, most of which resides in the 2p orbitals of oxygen atoms in the second solvation shell.

Despite the pronounced features between 2 and 3 Å (at which the lobes of the O 2p orbitals show up), the general outlook of the SOMO generated from the DFT calculation is similar to that given by one-electron models.[12,13] To demonstrate this, we note that in the simplest semicontinuum models,[12] the ground-state s-function of e_{hyd}^- is given by

$$\Psi_s(r) \propto \exp[-r/\lambda] \tag{6}$$

where λ is the localization radius of the electron. Fitting the radial density shown in Figure 4b to $4\pi r^2\Psi_s^2(r)$ gives the optimum $\lambda \approx 1.67$ Å, which is, indeed, close to the most probable location of the SOMO. As seen from Figures 3a and 2S, the SOMO for each particular snapshot is highly irregular. To better characterize the general shape of the SOMO, we elected to use multipole analysis. At the $l = 2$ pole, we characterize the charge distribution by a symmetrical gyration tensor,

$$\mathbf{G}_{ij} = \langle \mathbf{x}_i\mathbf{x}_j\rangle_\Psi - \langle \mathbf{x}_i\rangle_\Psi\langle \mathbf{x}_j\rangle_\Psi \tag{7}$$

where $\mathbf{x}_i = \{x, y, z\}$ and $\langle\ \rangle_\Psi$ stands for averaging over the SOMO density. This tensor is related to the (potentially experimentally observable) diamagnetic susceptibility tensor χ of the excess electron via $\chi = e^2/4m_ec^2\{\mathbf{G} - tr(\mathbf{G})1\}$. The gyration tensor $\mathbf{G}$ has eigenvalues (r_a^2, r_b^2, r_c^2), arranged so that $r_a < r_b < r_c$, that give the semiaxes of the gyration ellipsoid. The radius of gyration is then defined as

$$r_g^2 = r_a^2 + r_b^2 + r_c^2 = \langle r^2\rangle_\Psi - \langle r\rangle_\Psi^2 \tag{8}$$

The shape of the ellipsoid also can be characterized using the mean meridianal (e_m) and polar (e_p) eccentricities, defined as

$$e_m^2 = 1 - r_ar_b/r_c^2 \quad \text{and} \quad e_p^2 = 1 - r_a^2/r_b^2 \tag{9}$$

where for a truly spherically symmetric s-like wavefunction, the three semiaxes would be equal to the localization radius λ so that $e_m = e_p = 0$. The calculation gave a mean radius of gyration $r_g \approx 2.75$ Å (vs 2.04 Å in the MQC MD model), and the mean gyration ellipsoid is 1.48 Å × 1.58 Å × 1.69 Å (vs 1.07 Å × 1.17 Å × 1.28 Å in the MQC MD model). Thus, the shortest and the largest semiaxes of the gyration ellipsoid **G**, in the DFT/MQC MD model, are within 7% of the mean value; the mean eccentricities are $e_m \approx 0.42$ and $e_p \approx 0.33$. The gyration radius varies between 2.5 and 3 Å, and the principal semiaxes cover a wide range from 1.3 to 1.9 Å, and the eccentricities vary from 0.1 to 0.6 (Figure 5).

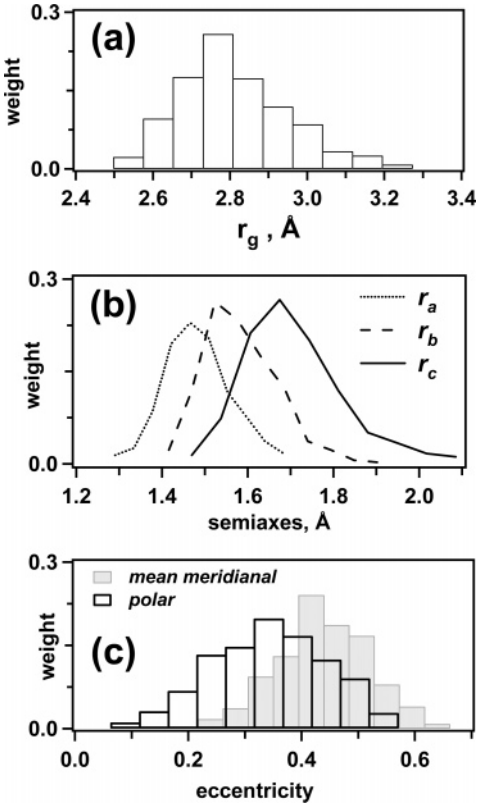

Figure 5. The histograms of (a) the gyration radius, r_g (eq 8), and (b) the three semiaxes $r_a < r_b < r_c$ of the gyration tensor, eq 7 (see the legend in the figure). The SOMO density is used to calculate this tensor. (c) The histograms of the mean meridianal (e_m, eq 9) and polar (e_p, eq 9) eccentricities of the gyration ellipsoid (see the legend in the figure). Wide distribution of these eccentricities illustrates great variation in the shape of the e_{hyd}^-.

The 2.75 Å average radius of gyration that we calculate is significantly greater than the experimental value of 2.5−2.6 Å estimated from moment analysis[33] of the optical spectrum[34] via eq 10,

$$r_g^2 \approx \frac{3\hbar^2}{2m_e}\int \mathrm{d}E\, E^{-1} f(E)/\int \mathrm{d}E\, f(E) \tag{10}$$

where $E = \hbar\omega$ is the transition energy and $f(E)$ is the oscillator strength of the corresponding electronic transition (see Section 3.2); it also greatly exceeds the estimate of ∼2.04 Å obtained directly from the MQC MD model using the Schnitker−Rossky electron−water pseudopotential.[24] We believe the discrepancy between our calculated value for the radius of gyration and the experimental one results from the MQC e_{hyd}^- trajectories, from which our snapshots were generated, having a cavity that was slightly too large. The experimental EPR and ESEEM data also suggest smaller cavities than in our MQC simulations (see ref 1 and Section 3.3).

3.2. Excited States and the Absorption Spectrum. As we saw in the preceding section, the excess electron's ground-state wavefunction, calculated with our many-electron method, is similar to the s-like ground-state wavefunctions seen in one-electron models,[8,24] but with important differences[1,35] (namely,

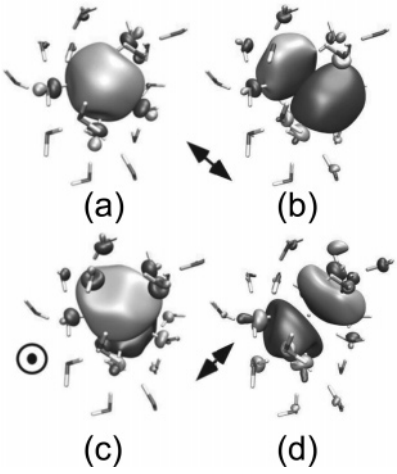

Figure 6. Isovalue surfaces of (a) the s-like ground-state (Hartree−Fock SOMO) and (b−d) p-like excited states of the e_{hyd}^- calculated for a typical embedded water anion cluster using CIS($N = 10$)/6-31+G* (isovalue $\pm$ 0.025a_0^{-3}) (see Section 3.2). Light shade is for positive and dark shade is for negative parts of the wavefunction. The directions of the transition dipole moments are indicated by arrows in b−d. These three directions are orthogonal for these lowest unoccupied states. A large color figure is shown in Figure 9S.

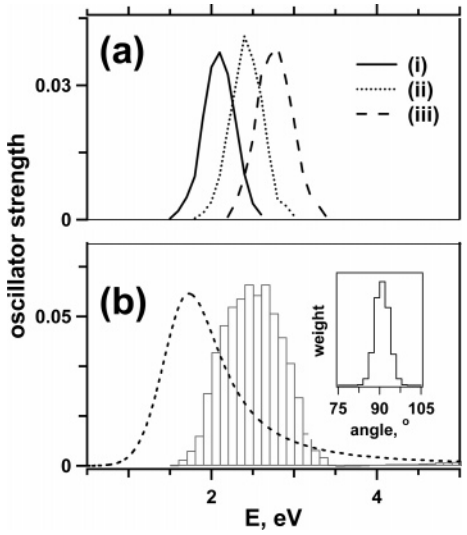

Figure 7. Simulated CIS($N = 10$)/6-31+G* spectra for embedded anion clusters (first two solvation shells only). The bin width for the histograms is 0.1 eV. (a) The histogram of oscillator strengths for the three lowest energy states ("p-states") i, ii, and iii. (b) The overall histogram for the first 10 excited states (single excitations only). In the inset in panel b, a histogram of the angles between the transition dipole moments μ_{0i} for the lowest three excited states is shown. The dashed curve is the experimental spectrum of the e_{hyd}^- in liquid water at 300 K.

the penetration of the excess electron into first solvation shell water molecules). One of the characteristic signatures of the e_{hyd}^- is its absorption spectrum in the visible, which one-electron models have previously assigned as arising predominantly from excitation of the s-like ground state to three p-like cavity supported excited states. To check the validity of this assignment, we now consider the excited states of the e_{hyd}^- calculated with our CIS/MQC method and how they contribute to its absorption spectrum in the visible.

Although CIS excited states are multideterminantal, for this problem, we can assign a single orbital to the excited excess electron since our CIS calculations showed that the most important electronic configurations for the three lowest-lying excited states of the e_{hyd}^- all involve excitations from the SOMO into virtual α-spin MOs (in fact, our CIS calculations showed that over 99% of the wavefunction involves this type of excitation). This allows us to define a single orbital for the excess electron in its *i*th excited state,

$$\chi_{\mathrm{CIS},i} = \sum_j c_{ij}\chi_j \qquad (11)$$

where c_{ij} is the CIS expansion coefficient for excited state i involving the excitation from the SOMO to virtual orbital j, χ_j. Thus, despite the mixing of the e_{hyd}^-'s wavefunction with the first-shell water frontier MO's, a one-electron picture of the e_{hyd}^- is quite robust.

Figure 6 shows isovalue surfaces for the excess-electron orbital (defined in eq 11) of the three lowest excited states taken from a typical snapshot in our CIS/MQC calculations. Also shown is the UHF SOMO (also the HOMO) for the ground-state wavefunction (Figure 6a), which displays features similar to the DFT SOMO (Figure 3). We clearly see the familiar dumbbell shape of a p orbital in the three lowest excited states (Figure 6, panels b−d), which have transition dipole moments from the ground state that point in roughly orthogonal directions, as indicated by the arrows on the figure. Like for the ground state (Section 3.1), we see significant mixing of the excited-state wavefunctions with the frontier orbitals of the first solvation shell waters, as well as a small amount of penetration into the second solvation shell waters. The p character of these excited states is also preserved in the polarization of the water frontier orbitals: the phase of the electron wavefunction in these orbitals on one side of the cavity has one sign, whereas the phase of the electron in the frontier orbitals straight across the cavity (in the direction of the transition dipole moment) assumes the opposite sign. We also see that the excited states are substantially larger than the s-like ground state (compare panels b−d to panel a in Figure 6) so that the excited-state wavefunctions overlap considerably with the first solvation shell waters. Thus, the orbital structure of the e_{hyd}^- as calculated by CIS resembles the s-like and p-like states of one-electron models but with some spillover of the electron density into the nearest water molecules.

Next we turn our attention to the absorption spectrum of the e_{hyd}^- in the visible. Figure 7 shows the spectrum calculated using the CIS($N = 10$)/6-31+G* method (Section 2) for embedded water anion clusters with $r_{cut} = 4.75$ Å. Since Figure 6 showed that the excited states of e_{hyd}^- are substantially more diffuse than the ground state, to ensure that our CIS calculations were reliable for these excited states, more than two water shells should have been treated explicitly with our embedding method. Unfortunately, including additional water shells is not feasible because of the excessive computational demands of such a calculation. Even though we are not certain that the excited-state wavefunctions are converged when only two solvent shells are treated explicitly, we can nevertheless draw some conclusions from our CIS calculations because the spectrum we calculate for the e_{hyd}^- using the CIS method does not change significantly when either one or two surrounding water shells are explicitly included (see Section S2). Thus, for the largest CIS calculation we can perform, the calculated absorption spectrum appears not to be sensitive to the size of the embedded cluster. Figure 7b shows that the CIS-calculated spectrum is significantly blue-shifted relative to experiment.[33] The best we can infer from these CIS calculations is that they reproduce the visible absorption spectrum of the hydrated electron about as well as traditional one-electron MQC calculations,[8,24] which also exhibit a significant blue shift relative to experiment (see below).

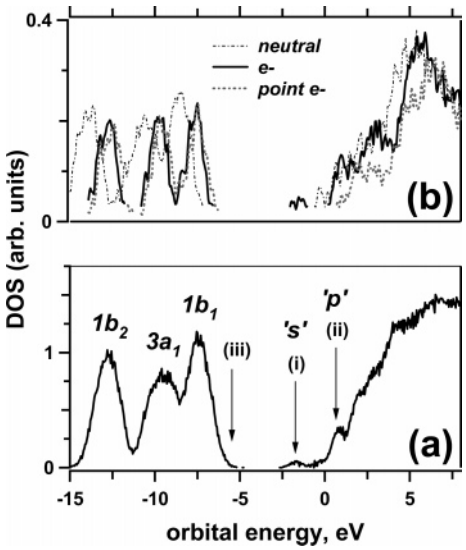

Figure 8. (a) Kohn−Sham density of states function, DOS (the occupancy number is shown) for e_{hyd}^- (r_{cut} = 4.75 Å). The arrows indicate the position of (i) the HOMO and (ii) the three lowest unoccupied states (shown separately in Figure 4S). (b) The same as panel a, for the embedded neutral water clusters (r_{cut} = 3.5 Å; dash dot curve), and the first solvation shell of the e_{hyd}^- (r_{cut} = 3 Å clusters): the solid curve is for the e_{hyd}^-, and the dashed curve is for a neutral water cluster (of the same geometry as water anion clusters) with a negative point charge placed at the electron's center of mass (*X*). The occupancy number for spin up orbitals is shown in panel b. The enlarged, color version of this plot is given in Figure 3S in the Supporting Information.

Indeed, we find that the electronic transitions responsible for the absorption spectrum are very similar to those found in the one-electron MQC calculations: our CIS-calculated absorption spectrum in the visible is dominated by three subbands centered at 2.09, 2.43, and 2.76 eV (Figure 7a) that correspond to excitation to the three p-like excited states, examined above, which have nearly orthogonal transition dipole moments (see the inset in Figure 7b). For comparison, a one-electron MQC model used by Schnitker et al.[8b] found the s- to p-subbands centered at 2.1, 2.5, and 2.9 eV. Each of the subbands displayed in Figure 7a carries an integral oscillator strength of ∼0.3, and the total integrated oscillator strength is ∼0.95, indicating that only the excess electron is excited in this region of the spectrum. Thus, the assignment of the absorption spectrum of the e_{hyd}^- in the visible as arising predominantly from exciting the s-like ground-state excess electron to a p-like excited state is confirmed with our multielectron model.

One feature of the experimental absorption spectrum of the e_{hyd}^- that has not been explained by one-electron models is a vacuum UV (VUV) band that peaks at 190 nm (6.5 eV) and has an onset around 220 nm.[19] Although our CIS calculations do not reveal the origin of this band, a plausible assignment for this absorption is revealed by examining the energy levels of the occupied water orbitals from our DFT calculations. Thus, in Figure 8a, we explore the density of states (DOS) of the e_{hyd}^- for our embedded water cluster anions (with r_{cut} = 4.75 Å). To obtain the DOS from the DFT calculations, we calculated histograms of the KS eigenvalues for the occupied and virtual eigenstates of both spin orientations (in our convention, the SOMO is an α function). The DOS exhibits two features near the bottom of the "conduction band" that are shown separately in Figure 4S(a). Feature i results from the highest occupied α-orbital that is located ∼−1.69 eV below the vacuum energy (the DOS maximum is at −1.8 eV vs −1.75 eV given by the ab initio molecular dynamics calculation of Boero et al.).[17] Feature ii derives from the three lowest unoccupied molecular α-orbitals (LUMO, LUMO + 1, and LUMO + 2), which have centroids at 0.42, 0.65, and 0.86 eV, respectively. It is natural to make a correspondence between these three states and the three nondegenerate p-like states observed in our CIS calculations. Indeed, as we show in Section S3, isosurfaces for these unoccupied KS orbitals resemble the p-like orbitals shown in Figure 6. Feature iii in the DFT density of states results from a band of HOMO-1 orbitals that are composed of $^1b_1$ orbitals of the water molecules in the first solvation shell; a typical such HOMO-1 orbital is shown in Figure 3b. Our calculations suggest that the onset of this band starts 5.75 eV below the vacuum level and it has its first peak at −7.5 eV. An electronic transition from this band of water $1b_1$ orbitals into the HOMO would occur at ∼5.95 eV (∼210 nm), which is close to the experimentally observed absorption band of the e_{hyd}^- at 190 nm.[19] Thus, our hybrid DFT/MQC MD model provides an assignment for the observed VUV band of the e_{hyd}^-. Our CIS calculations did not reveal any significant absorption in this region because this transition likely has significant multielectron character that is not accounted for at the CIS level of theory.

To better understand the origin of the transition at 5.95 eV, in Figure 8b we plot both the DOS function for embedded *neutral* clusters (using r_{cut} = 3.5 Å from a central oxygen atom) and the DOS for the anionic clusters including only a point negative charge at *X* (instead of a full description of the excess electron) using only the first solvation shell (r_{cut} = 3 Å); we also include the DOS of embedded small water anions also using only the first solvation shell. Figure 8 shows that the DOS of both the neutral and small anion clusters have three peaks that correspond to the $1b_2$, $3a_1$, and $1b_1$ orbitals of *neutral* water molecules (see Figure 20 in ref 36 for a sketch of these orbitals); the respective bands for these orbitals have been observed experimentally in the photoelectron spectra of liquid water by Faubel and co-workers.[36] Figure 8 also shows that the presence of a point negative charge in the cavity causes a Stark shift of the eigenvalues toward the midgap by ∼1.1 eV. The most prominent feature in the DOS of the anionic clusters corresponds to the upshifted $1b_1$ band (that is, the HOMO-1 orbital) that arises from the O 2p orbital in the water molecule that is perpendicular to its plane (Figure 3b). It turns out that even a point charge placed at the cavity center can fully account for this upshift; a full wavefunction description of the intracavity electron does not significantly change the calculated DOS for occupied states with energies more negative than −3 eV.

To summarize this section, our hybrid DFT/- and CIS/MQC MD calculations qualitatively account for many of the experimentally observed features of the hydrated electron, including its absorption band in the visible and the second band in the VUV. The three lower unoccupied states are nondegenerate and correspond to p-type orbitals oriented in roughly orthogonal directions. The splitting between the corresponding p-subbands and their widths are comparable to the those reported in both MQC MD[9] and ab initio molecular dynamics calculations,[17] despite the qualitative differences among these three models. Although the multielectron calculations yield a somewhat different orbital structure for the "p-states" than the MQC MD and other one-electron models,[8−11] the absorption spectrum still resembles the one simulated using such one-electron models. Thus, our results suggest that the optical spectrum alone cannot be used to validate or invalidate models for the e_{hyd}^-. Instead, other experimental features, such as hfcc parameters determined using magnetic resonance methods,[1−6] or vibrational parameters

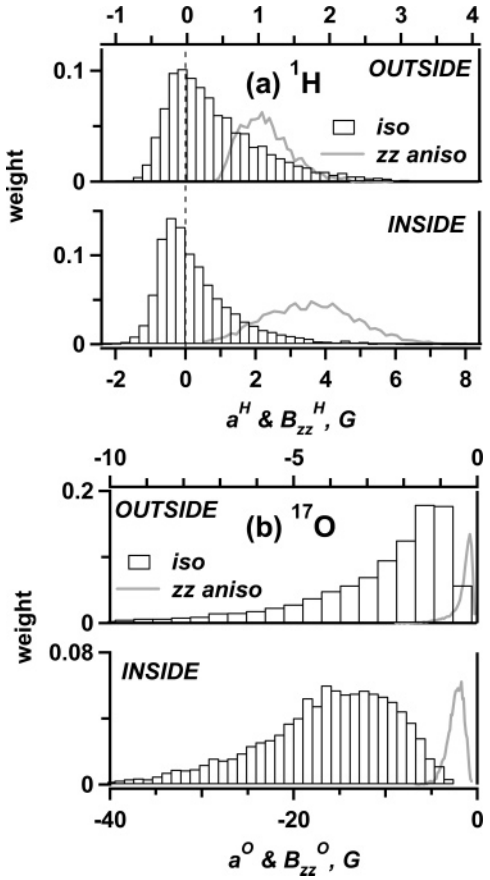

Figure 9. Histograms for isotropic (a^H and a^O, empty bars) and anisotropic (B_{zz}^H and B_{zz}^O, gray curves) hyperfine coupling constants for embedded water anions (for ^{1}H and ^{17}O nuclei, respectively) (a) for hydrogens of the first solvation shell and (b) for oxygens of the first and the second solvation shells (see Section 2.2 for the definition). The "outside" histogram is plotted to the top, the "inside" one is plotted to the bottom. The mean values are given in Table 1. Since the distribution functions for isotropic hfcc's are skewed, the most probable values are significantly lower than the mean ones. Observe the broad distribution of B_{zz}^H for H_a nuclei in part a, lower panel.

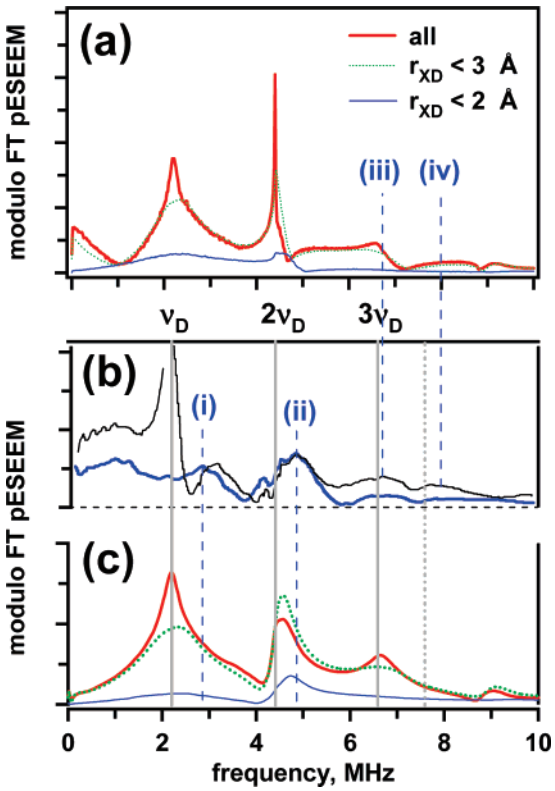

Figure 10. Modulo FT primary ESEEM spectra for trapped electron; the NMR frequency ν_D of the neutron in the X-band is 2.2 MHz. The first, the second, and the third harmonics of this frequency are indicated by solid vertical bars in panels b and c; the dashed bold line indicates the frequency of 7.6 MHz used for rejection filtering of ^{23}Na modulation in the experimental spectra of ref 6. (a, c) Simulated spectra (the matrix nuclei are not taken into account) and (b) the experimental data from ref 6 for the trapped electron in low-temperature 10 M $Na^{16}OD/D_2{}^{16}O$ glass. In panels a and c, the bold red curve is for the simulation that takes all deuterons in the cluster (the first and the second solvation shell), the dotted green curve is from all D_{in} nuclei, and the thin blue curve is for D_{out} nuclei with r_{XD} < 2 Å). In panel b, the thin black and the bold blue curves correspond to the experimental spectra before and after the rejection filtering, respectively (intended to suppress the signal from matrix deuterons). Lines (i) and (ii) correspond to $\nu_{\alpha,\beta}^{\perp}$ and $\nu_\alpha + \nu_\beta$ frequencies, respectively (see Appendix B of ref 1). Curves c are the same as a, after taking into account the distortions introduced due to the loss of the spin echo modulation pattern during the dead time of the EPR spectrometer and the broadening of the spectra due to the electron relaxation.

obtained from resonance Raman[20,21] are needed to refine our theoretical understanding of the hydrated electron.

3.3. EPR and ESEEM Spectra. EPR and ESEEM spectroscopy provide estimates for hfcc's that strongly depend on the cavity geometry and amount of spin density of the excess electron overlapping with magnetic nuclei (^{1}H, ^{2}H, and ^{17}O) in the nearby water molecules. In Part 1 of this study,[1] we found that in water cluster anions that trap the electron internally, the excess spin and charge density are localized mainly on the OH groups of the first solvation shell. For the embedded cluster anions examined in the present study, this same type of distribution is also seen, as shown in Figure 11S, which exhibits histograms of the atomic spin ($\rho_s^{H,O}$, panel a) and charge ($\rho_c^{H,O}$, panel b) densities for our $r_{cut} = 4.75$ Å clusters. For comparison, Figure 11S(b) shows the charge distribution on individual neutral water molecules in the matrix (with $\langle \rho_c{}^H \rangle \approx 0.36$). Examination of this latter plot suggests that for the anionic water clusters, both the O atoms in the second solvation shell and the H_{out} atoms in first solvation shell have an atomic charge that is within 0.02*e* of what is observed for bulk water molecules. For the solvating OH groups, however, the charge on the H_{in} hydrogens is 0.2*e* more negative than in neutral water, and the charge on the first-shell oxygen atoms is 0.17*e* more positive than in neutral water. Figure 11S(a) also shows that the spin density follows a similar trend: the spin density on the H_{out} nuclei is small and on the oxygen nuclei in the second shell is almost negligible; the most probable values for the spin density on the H_{in} and the first-shell O atoms are $+0.1 \pm 0.05$ and -0.04 ± 0.01, respectively. It is noteworthy that the distribution of the spin density for the H_{in} atoms is very broad, spanning a range from -0.2 to $+0.4$.

Figure 9a and b shows histograms of the isotropic and anisotropic components of the hyperfine coupling tensor for H_{in} and H_{out} protons and ^{17}O nuclei, respectively. There is a broad distribution of calculated hfcc values, and the distributions for the isotropic hfcc's are skewed, so the mean values are quite different from the most probable ones (Table 1). The mean values of a^O for ^{17}O nuclei in the first and the second solvation shells are ~ -15 G and ~ -2.1 G, respectively. The correlation plot of these isotropic hfcc's vs $X-O$ distance, given in Figure 12S(a), shows that to a first approximation, $a^O \propto \exp(-2r_{XO}/\lambda_O)$, where $\lambda_O \approx 1.59$ Å is close to the localization radius λ of the SOMO (eq 6). No such correlation is obvious for the protons, since the hfcc depends on the orientation of the O 2p orbital to

which the electron in the H 1s orbital is coupled. The correlation plot of B_{zz}^{H} for the H_{in} protons given in Figure 12S(b) shows that the point dipole approximation, $B_{zz}^{H}(G) \approx 57.6/r_{XH}^{3}$ [1] (for $X-H_{in}$, distances in units of Å), holds well for $B_{zz}^{H} < 6$ G. This is due to both the relative sphericity of the SOMO (with its large mean coordination number n_H) and the preferential orientation of OH groups toward the cavity; by contrast, in model anion clusters with low coordination number of the cavity electron and d-orientation of water molecules (see Part 1),[1] there is considerable deviation from the point dipole approximation.

Using the calculated hfcc tensors, one can estimate the contributions from both ^{1}H and ^{17}O nuclei to the second moment, $M_2^{H,O}$, of the EPR spectra (Table 1 and Figure 13S). The contribution to this moment from each magnetic nucleus is given by $1/3I(I+1)(a^2 + 2T_{\perp}^{2})$, where I is the nuclear spin. For protons (deuterons), the second, dipolar, term in the last factor prevails. For $NaOH/H_2O$ glasses, the proton contribution, M_2^{H}, was determined experimentally to be between 21 and 23 G^2.[4,6] Our hybrid calculation gives a mean value of 17.3 G^2 (a histogram of our calculated values for M_2^{H} is shown in Figure 13S(b)); ~80% of the mean value comes from the anisotropic hyperfine interaction. There is also an additional contribution to M_2^{H} of ~0.8 G from the remote matrix protons, which can be treated using the point−dipole approximation. Our slightly low estimate for M_2^{H} is likely due to the overestimated cavity size from our MQC MD simulations, which gives $\langle r_{XH}\rangle_{in} = 2.4$ Å for the H_{in} protons; in contrast, experimental estimates for the cavity size from EPR[4] and ESEEM[2,6] are 2−2.2 Å. The fact that our calculations are based on clusters with too large a cavity also results in a relatively low estimate for $\langle B_{zz}^{H}\rangle_{in} \approx 3.7$ G; the experimental estimates of this quantity are 6−7 G.[2,6] It is worth noting that due to the very steep (cubic) dependence of the dipole component of the hfcc tensor on r_{XH}, even a small error in the cavity size causes a large error in the estimates for B_{zz}^{H}. (The fact that our cavity size is likely too large is also evident when comparing our calculated radius of gyration, r_g, for the electron to experimental estimates, as noted in Section 3.1).

Figure 14S(a) shows the simulated EPR spectrum, which is close to Gaussian in shape and which looks much like the experimental spectrum in the alkaline glasses.[4] The peak-to-peak line width for ΔB_{pp} of 9.1 G that we calculate compares well with the experimental estimate of 9.5 ± 0.5 G reported by Astashkin et al.[6] The EPR spectra for ^{17}O-enriched samples can also be accounted for by using these hfcc's (Section S4 and Figure 14S(b)).

We turn next to the experimental ESEEM results for the e_{hyd}^{-} in $NaOD/D_2O$ glasses, which are shown in Figure 10 (see Appendices A and B of Part 1 for a brief introduction to ESEEM spectroscopy and how such spectra are simulated). Figure 10a shows simulated Fourier transform modulo primary (p-) ESEEM spectra; in these calculations, we did not consider the (magnetically) weakly coupled matrix deuterons. These calculations reflect the "ideal" spectra that would be obtained assuming that the EPR spectrometer has no dead time and that there is no relaxation that narrows the observation window. In Figure 10c, however, we include such effects, assuming a dead time of 250 ns and a relaxation time of 2 μs, as in the experiments of Astashkin et al.)[6] For comparison, the experimental spectra are shown in Figure 10b. Since the weakly coupled matrix nuclei yield very strong signals at ν_D and $2\nu_D$ (where $\nu_D \approx 2.2$ MHz is the NMR frequency of the deuteron in the magnetic field of EPR spectrometer), Astashkin et al.[6] used rejection filtering at these frequencies to single out the more strongly coupled D_{in} nuclei. These authors also used additional rejection filtering at a frequency of 7.6 MHz to reduce the (weak) modulation signal from magnetic ^{23}Na nuclei. We note, however, that all the various filtering also serves to distort the spectrum. The two peaks marked (i) and (ii) in Figure 10b correspond to $\nu_{\alpha,\beta}^{\perp} \approx |\nu_D \pm (a^D + T_{\perp}^{D})/2|$ and the sum frequency $\nu_\alpha + \nu_\beta \approx 2\nu_D(1 + [T_{\perp}^{D}/2\nu_D]^2)$, where the indices α and β refer to the two orientations of the electron spin with respect to the magnetic field. Since the parameters a^D and $T_{\perp}^{D} \approx -B_{zz}^{D}/2$ are widely distributed (see Figure 9a for the proton hfcc's) the corresponding lines are broad. The reported estimates of "mean" hfcc's correspond to the positions of peaks that are not well defined for such broad lines. Simulation of the FT pESEEM spectrum using such "mean" values for one, two,[6] or six[2] magnetically equivalent deuterons do not yield traces that resemble the experimental ones (Figure B1 in ref 1 and ref 6).

By contrast, our simulation based on our hybrid many-electron calculation involves all of the deuterons coupled to the electron and averages over all such configurations. To distinguish the contributions from different groups of nuclei, Figure 10a and c show three traces plotted together: a trace for all deuterons in the first and the second solvation shells, a trace for only the D_{in} nuclei, and a trace for just the close-in D_{in} nuclei with $r_{XD} < 2$ Å (for which $\langle a^H\rangle \approx +0.68$ G and $\langle B_{zz}^{H}\rangle \approx 5.6$ G in the protonated sample). Since the deuterons in the second solvation shell are only weakly coupled, these nuclei give narrow lines in the FT pESEEM spectra that are superimposed on the broad signals from the D_{in} nuclei. At high frequencies, there are also two lines (marked (iii) and (iv) that correspond to the third harmonic of the NMR frequency and a combination frequency, respectively, which are clearly seen in Figure 10b. These characteristic features were missing from all previous reconstructions of the ESEEM spectra. We note that no rejection filtering was used for our *simulated* ESEEM spectra, so the sharp lines from the distant deuterons at ν_D and $2\nu_D$ are superimposed on the broader lines of D_{in} deuterons. As seen from the comparison of panels b and c of Figure 10, the simulated FT pESEEM spectrum matches the experimental spectrum in the overall shape, although the center bands are shifted to lower frequency. This is, once again, a consequence of overestimated cavity size in the MQC MD model. Longer $X-D_a$ distances result in smaller dipolar coupling and, thus, a lower $\nu_\alpha + \nu_\beta$ frequency. By choosing only those nuclei for which $r_{XD} < 2$ Å, however, it is possible to match the simulated and the experimental ESEEM spectra in both the positions of bands (i) and (ii) and their widths, as seen in Figure 10c). The results obtained in Part 1 of this study[1] for model octahedral clusters suggest that the matching is possible only for $X-D_{in}$ distances of 1.9−2.2 Å. Although the difference between this optimum distance of r_{XH} and the MQC MD average of 2.4 Å is small, it is sufficient to reduce $T_{\perp}^{D}$, which steeply depends on this distance. Other than this, our hybrid DFT/MQC MD model appears to account for all of the experimentally observed features of EPR and ESEEM spectra of the e_{hyd}^{-} trapped in alkaline ice.

3.4. Vibrational Spectra. In resonance Raman spectroscopy, only those vibrational modes that are significantly displaced upon electronic excitation show resonance enhancement;[20,21] thus, resonance Raman spectroscopy provides an excellent probe of the water molecules in the immediate vicinity of the hydrated electron. The vibrational peaks in the experimental resonance Raman spectra of the e_{hyd}^{-} all exhibit significant downshifts relative to the peaks present in neat water without an excess

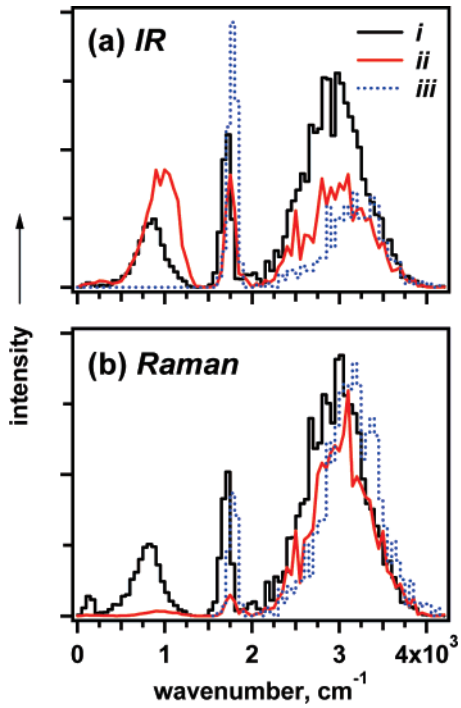

Figure 11. Simulated (a) IR and (b) Raman spectra (B3LYP/6-31+G** model), for (i) embedded water anion clusters (r_{cut} = 3 Å, i.e., the first solvation shell only; black curve), (ii) embedded neutral clusters (r_{cut} = 3.5 Å as measured from O atoms of one of water molecules; red curve), and (iii) embedded single water molecules (dashed blue curve, see the legend in the upper panel). Band centroids (eq 3) are given in Table 2. There is a notable blue shift relative to experiment in all three major vibration bands. In panel b, trace iii is scaled by a factor of 4 to facilitate the comparison.

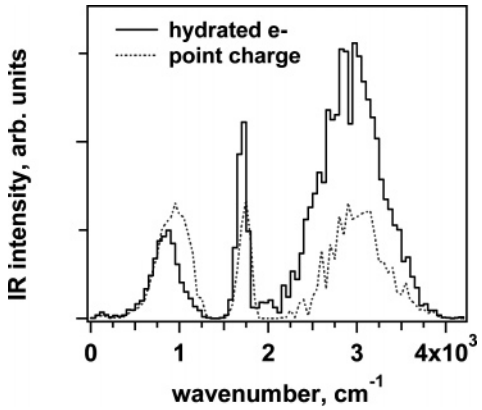

Figure 12. Simulated IR spectrum for an "excess electron." The dashed curve is for clusters with a negative point charge embedded at the position of the electron center of mass (*X*) in the MQC model, the solid curve is for embedded water anion clusters of the same geometry, that is, reproducing Figure 11a, trace i. See Table 2 for positions of centroids.

electron. According to Tauber and Mathies,[20] the resonance Raman peak position for the e_{hyd}^- in H_2O (vs those for bulk water), in cm^{-1}, are librations at 410 (vs 425−450), 530 (vs 530−590), 698 (vs 715−766); the H−O−H bend at 1610 (vs 1640); and the H−O stretches at 3100 (vs 3420). Thus, the downshift of the bend mode, which exhibits a narrow, symmetric line, is ∼30 cm^{-1}, and the downshift of the stretch mode (as estimated by the shift of the half-maximum of the broad, asymmetric line) is ∼200 cm^{-1}. The question we address in this section is how to account for these experimentally observed vibrational downshifts.

There have been previous ab initio and DFT calculations for gas phase $O(H_2O)_n^-$ anions[15,16,37] and related $(H_3O)(H_2O)_n$[38] clusters in which the experimentally observed downshifts for the bending and stretching modes were qualitatively reproduced, suggesting that electron sharing with the nearby water molecules is the key to understanding the downshifts. For electrons trapped at the surface of small water anion clusters (that also exhibit downshifts of the vibrational modes), Herbert and Head-Gordon[39] have recently suggested that these downshifts originate from donor−acceptor stabilization between the unpaired electron and O−H σ^* orbitals. For the e_{hyd}^-, this type of penetration of the electron density into anibonding orbitals of water molecules had been previously suggested by Tauber and Mathies[21] and Mizuno et al.[22]. DFT calculations for Kevan's octahedral model (Appendix C in Part 1)[1] indicate that sharing of the electron density by O 2p orbitals in this model water anion would quantitatively reproduce the observed downshifts for H−O and H−O−H vibrational modes in this octahedral cluster for $r_{XH} \approx$ 2−2.1 Å.

These gas-phase cluster calculations are suggestive, but the hallmark of liquid water is its network of H-bonds, and this network is absent in such calculations. Park et al.[18] have calculated the H-atom velocity autocorrelation spectral density for six water molecules in the first solvation shell of the e_{hyd}^- in *liquid* water. Their hybrid model explicitly treated the electrons in the water molecules using ionic pseudopotentials and downshifts of ∼40 cm^{-1} for H−O−H modes and ∼110 cm^{-1} for O−H modes were observed; the downshifts of the low-frequency modes (<1000 cm^{-1}) were less apparent. The authors attributed these downshifts to the "attractive interaction between the electron and neighboring H atoms." In this section, we seek to verify and extend these results using a more explicit treatment of the water molecules with our embedded clusters, whose geometry should be representative of the liquid.

As described in Section 2, we calculated the vibrational modes of the e_{hyd}^- using a local harmonic approximation for our embedded water anion clusters. Importantly, the experimental data are *resonance* Raman spectra,[20,21] whereas the simulated spectra are *regular* IR and Raman spectra (which was also the case for calculations of Park et al.).[18] For large embedded water anion clusters, both the vibrations of the OH groups forming the cavity and the vibrations in water molecules in the second solvation shell are present in the spectrum, whereas the experimental resonance Raman spectrum selects only those modes that are significantly displaced upon electronic excitation of the electron, which are presumably those of the first-shell water molecules. Since the calculation of a *resonance* Raman spectrum was not feasible, we examined only relatively small clusters with r_{cut} = 3 Å (of 5−8 water molecules) in order to selectively observe the vibrations of water molecules in the first solvation shell.

Our simulated vibrational spectra are shown in Figures 11 and 12, and the vibrational band centroids are summarized in Table 2. For comparison, Figure 11a shows the calculated IR spectrum for a MD simulation of neat SPCf water. Traces ii and iii in Figure 11, respectively, show that the vibrational bands of medium-size neutral clusters are somewhat different from those of embedded isolated water molecules. Despite the fact that the absolute positions of the vibrational features do not match experiment, Figure 11 shows that the downshifts of these bands in the presence of the excess electron are well described by our hybrid calculation: we see downshifts of the librational modes at 750 cm^{-1}, the H−O−H bending mode at 1700−1750 cm^{-1}, and the O−H stretch modes around 3000 cm^{-1} that are

in reasonable agreement with the resonance Raman experiments.[20] To test whether these vibrational downshifts originate simply through electrostatic interactions with the negative charge inside the cavity, we also calculated the IR-Raman spectra for embedded neutral clusters having exactly the same geometry as the water anion clusters but with a point negative charge at *X*. Figure 12 presents a comparison of the IR spectra for our embedded water anion clusters (solid curve) and such "point charge" clusters (dashed curve); the corresponding band centroids are given in Table 2. The comparison clearly suggests that electrostatic interactions alone cannot account for the downshift of the vibration bands; it is the mixing of the excess electron's wavefunction with the frontier molecular orbitals of the first-shell water molecules that weakens the bonds and leads to the lower vibrational frequencies. The magnitude of our calculated downshifts can be estimated from the data in Table 2. The calculated downshift for the H−O−H bending mode is ∼50−60 cm^{-1} (as compared to the experimental estimate of 30 cm^{-1});[20,21] the calculated downshift for the O−H stretching modes is 80−180 cm^{-1} (as compared to the experimental estimate of 200 cm^{-1} for the band center).[20] Thus, although our DFT estimates for band downshifts using *optimized* octahedral water clusters are closer to experiment,[1] the hybrid model, despite its many approximations, accounts reasonably well for the observed features of the resonance Raman spectra of the e_{hyd}^-.

The plots of vibrational density of states (VDOS) for anion and neutral clusters (Figure 15S) reveal a large peak at 100 cm^{-1} (3 THz) corresponding to low-amplitude motions of water molecules relative to the cavity (which is in the same 25−75 cm^{-1} range as the symmetric "breathing" mode predicted by Copeland et al.[40]). No definitive signature of these low-frequency vibrations was found in autocorrelation functions for orbital and transition energies and the radius of gyration; rapid exchange of water molecules is likely to hide these modes.

4. Concluding Remarks

In this paper, we have shown that a combined DFT/- and CIS/MQC MD approach can account, at least semiquantitatively, and in many instances, quantitatively, for many of the experimentally observed features of the ground-state e_{hyd}^-: these include the absorption bands in the visible and the VUV, the vibrational spectra, and the EPR and ESEEM spectra. The salient feature found from our multielectron model of the e_{hyd}^- is that a considerable (∼18%) fraction of the excess electron's density resides in the frontal O 2p orbitals of oxygen atoms in the hydrating OH groups. Not only does this sharing not contradict experimental observations, but it also naturally accounts for the magnetic resonance spectra and the downshifts of the water vibrational frequencies seen in resonance Raman experiments on the e_{hyd}^-.

Despite the extensive spin and charge sharing, the average ground and excited-state orbitals resemble in their general appearance the s- and p-like states in the one-electron models. This rationalizes the success of such models in explaining the energetics and main spectral features of the e_{hyd}^-. Our hybrid calculations show that 60% of the density of the ground "s-state" is confined inside the cavity, and 80% is confined within the first solvation shell. This tight electron localization justifies the embedded cluster approach used in this study. Our calculations also reproduce some other features seen in one-electron models, such as the facts that the gyration ellipsoid is aspherical, the lower three excited "p-states" are nondegenerate and extend beyond the solvation cavity, and the transition dipole moments to these three "p-states" are nearly orthogonal. Our DFT calculations also provide an assignment for the 190 nm absorption band of the e_{hyd}^-.[19] The presence of the negative charge inside the cavity makes the orbital energies of the valence electron in water molecules in the first solvation shell ∼1.1 eV more positive than in liquid water. We thus assign the VUV band of the e_{hyd}^- as originating from an electron transition from a Stark-shifted $1b_1$ orbital of the first-shell water molecules to the HOMO.

We also see that spin sharing of the excess electron by O 2p orbitals of the first and, to a lesser degree, the second solvation shells results in large hyperfine coupling constants for ^{17}O nuclei in these molecules. In Section S4, we demonstrate how EPR results of Schlick et al.[5] for ^{17}O-enriched alkaline glass samples can be accounted for in the DFT model. The same calculations also account for all of the important features of the ESEEM spectra,[2,6] including line widths and the presence of high-frequency bands that up until now have not been explained. We believe that the residual disagreement between our calculations and experiment stems from the fact that our MQC MD calculations are based on a pseudopotential[24] that slightly overestimates the size of the solvation cavity, resulting in reduced isotropic and anisotropic hfcc's as compared to the experiment. Alternatively, the structure of the alkaline glass might be different from liquid water, resulting in tighter solvation cavities.

Our calculations also yielded significant downshifts for all of the vibrational modes in the water molecules forming the solvation cavity. None of the shifts observed in our model can be accounted for by a simple electrostatic interaction with a point charge at the cavity center: instead, the observed changes in the vibrational modes result from the presence of the excess electron density in the O 2p orbitals. The magnitude of our calculated downshifts compare favorably to those determined experimentally.[20] Our conclusion that charge transfer and sharing of the electron with water molecules is the prime cause for the downshifts is in accord with several recent suggestions for e_{hyd}^-[20,21] and its gas phase analogs.[37,39]

In conclusion, we believe that our hybrid DFT(CIS)/MQC MD model not only captures all of the salient features of one-electron models of the e_{hyd}^- but also presents a further refinement of the picture of electron hydration in general and provides a consistent explanation of those properties of the e_{hyd}^- that cannot be addressed using one-electron models. Our DFT-(CIS)/MQC MD model suggests that the traditional cavity picture of the e_{hyd}^- is incomplete: the excess electron cannot be considered fully independently of the valence electrons in water molecules. Thus, we view the "hydrated electron" as a kind of multimer radical anion[35] of water in which the electron wavefunction is shared between the cavity and the water molecules forming it. Just such a picture has been advocated by Symons[41] and, later on, by Kevan.[3]

Acknowledgment. I.A.S. thanks C. Elles, S. E. Bradforth, A. Boutin, J. M. Herbert, A. Khan, W. Domcke, A. Nilsson, J.-P. Renault, and D. M. Bartels for useful discussions. This work was supported by the Office of Science, Division of Chemical Sciences, US-DOE under contract No. DE-AC-02-06CH11357. B.J.S., W.J.G., and R.E.L. gratefully acknowledge the support of the National Science Foundation under grant number CHE-0603776.

Supporting Information Available: A PDF file containing Sections S1−S4 and Figures 1S−15S with captions. This

material is available free of charge via the Internet at http://pubs.acs.org.

References and Notes

(1) Shkrob I. A. *J. Phys. Chem. A* **2007**, Part 1 of this series.

(2) Narayana, P. A.; Bowman, M. K.; Kevan, L.; Yudanov, V. F.; Tsvetkov, Yu. D. *J. Chem. Phys.* **1975**, *63*, 3365.

(3) Kevan, L. *J. Phys. Chem.* **1978**, *82*, 1144.

(4) Helbert, J.; Kevan, L.; Bales, B. L. *J. Chem. Phys.* **1972**, *57*, 723. Yoshida, H.; Feng, D.-F.; Kevan, L. *J. Chem. Phys.* **1973**, *58*, 3411. Bales, B. L.; Helbert, J.; Kevan, L. *J. Phys. Chem.* **1974**, *78*, 221. Bales, B. L.; Bowman, M. K.; Kevan, L.; Schwartz, R. N. *J. Chem. Phys.* **1975**, *63*, 3008.

(5) (a) Schlick, S.; Narayana, P. A.; Kevan, L. *J. Chem. Phys.* **1976**, *64*, 3153. (b) Schlick, S.; Kevan, L. *J. Phys. Chem.* **1977**, *81*, 1083.

(6) Astashkin, A. V.; Dikanov, S. A.; Tsvetkov, Yu. D. *Chem. Phys. Lett.* **1988**, *144*, 258. Dikanov S. A.; Tsvetkov, Yu. D. *Electron Spin Echo Envelope Modulation (ESEEM) Spectroscopy*; CRC Press: Boca Raton, 1992; Chapter 133, pp 244−251.

(7) See: Chandler, D.; Leung, K. *Annu. Rev. Phys. Chem.* **1994**, *45*, 557 for a review. Schnitker, J.; Rossky, P. J. *J. Chem. Phys.* **1986**, *86*, 3471. Wallqvist, A.; Thirumalai, D.; Berne, B. J. *J. Chem. Phys.* **1986**, *86*, 6404. Romero, C.; Jonah, C. D. *J. Chem. Phys.* **1988**, *90*, 1877. Wallqvist, A.; Martyna, G.; Berne, B. J. *J. Phys. Chem.* **1988**, *92*, 1721. Miura, S.; Hirata, F. *J. Phys. Chem.* **1994**, *98*, 9649.

(8) (a) Webster, F. J.; Schnitker, J.; Frierichs, M. S.; Friesner, R. A.; Rossky, P. J. *Phys. Rev. Lett.* **1991**, *66*, 3172. Murphrey, T. H.; Rossky, P. J. *J. Chem. Phys.* **1993**, *99*, 515. (b) Schnitker, J.; Motakabbir, K.; Rossky, P. J.; Friesner, R. A. *Phys. Rev. Lett.* **1988**, *60*, 456.

(9) Schwartz, B. J.; Rossky, P. J. *J. Chem. Phys.* **1994**, *101*, 6917; *J. Phys. Chem.* **1994**, *98*, 4489; *Phys. Rev. Lett.* **1994**, *72*, 3282; *J. Chem. Phys.* **1994**, *101*, 6902. Rosenthal, S. J.; Schwartz, B. J.; Rossky, P. J. *Chem. Phys. Lett.* **1994**, *229*, 443.

(10) Wong, K. F.; Rossky, P. J. *J. Phys. Chem. A* **2001**, *105*, 2546.

(11) Borgis, D.; Staib, A. *Chem. Phys. Lett.* **1994**, *230*, 405. Staib, A.; Borgis, D. *J. Chem. Phys.* **1995**, *103*, 2642. Borgis, D.; Staib, A. *J. Chim. Phys.* **1996**, *93*, 1628; *J. Chem. Phys.* **1996**, *104*, 4776; *J. Phys.: Condens. Matter* **1996**, *8*, 9389. Staib, A.; Borgis, D. *J. Chem. Phys.* **1996**, *104*, 9027. Borgis, D.; Bratos, S. *J. Mol. Struct.* **1997**, *1997*, 537. Nicolas, C.; Boutin, A.; Levy, B.; Borgis, D. *J. Chem. Phys.* **2003**, *118*, 9689. Coudert, F.-X.; Boutin, A. *Chem. Phys. Lett.* **2006**, *428*, 68.

(12) Fueki, K.; Feng. D.-F.; Kevan, L. *J. Phys. Chem.* **1970**, *74*, 1977. Fueki, K.; Feng. D.-F.; Kevan, L.; Christoffersen, R. E. *J. Phys. Chem.* **1971**, *75*, 2297. Fueki, K.; Feng. D.-F.; Kevan, L. *J. Am. Chem. Soc.* **1973**, *95*, 1398. Feng. D.-F.; Ebbing, D.; Kevan, L. *J. Chem*. Phys. **1974**, *61*, 249.

(13) Ogg, R. A. *J. Am. Chem. Soc.* **1940**, *68*, 155; *J. Chem. Phys.* **1946**, 14, 114 and 295; *Phys. Rev.* **1946**, *69*, 243 and 668; Jortner, J. *J. Chem. Phys.* **1959**, *30*, 839. Kestner, N. R. In *Electrons in Fluids*; Jortner, J., Kestner, N. R., Eds.; Springer-Verlag: New York, 1973; pp 1.

(14) Newton, M. D. *J. Phys. Chem.* **1975**, *79*, 2795; Clark, T.; Illing, G. *J. Am. Chem. Soc*. **1987**, *109*, 1013.

(15) Kim, K. S.; Park, I.; Lee, K.; Cho, K.; Lee, J. Y.; Kim, J.; Joannopoulos, J. D. *Phys. Rev. Lett*. **1996**, 76, 956. Kim, K. S.; Lee, S.; Kim, J.; Lee, J. Y. *J. Am. Chem. Soc*. **1997**, *119*, 9329. Lee H. M.; Kim, K. S. *J. Chem. Phys.* **2002**, *117*, 706. Lee, H. M.; Suh, S. B.; Kim, K. S. *J. Chem. Phys.* **2003**, *118*, 9981; *J. Chem. Phys.* **2003**, *119*, 187.

(16) Khan, A. *J. Chem. Phys.* **2006**, *125*, 024307; *Chem. Phys. Lett*. **2005**, *401*, 85; *J. Chem. Phys.* **2003**, *118*, 1684; *J. Chem. Phys.* **2003**, *121*, 280. Herbert, J. M.; Head-Gordon, M. *J. Phys. Chem. A* **2005**, *109*, 5217; *Phys. Chem. Chem. Phys.* **2006**, *8*, 68; Proc. Natl. Acad. Sci U.S.A. **2006**, *103*, 14282.

(17) Boero, M.; Parrinello, M.; Terakura, K.; Ikeshoji, T.; Liew, C. C. *Phys. Rev. Lett.* **2003**, *90*, 226403.

(18) Park, I.; Cho, K.; Lee, S.; Kim, K. S.; Joannopoulos, J. D. *Comp. Mater. Sci.* **2001**, *21*, 291.

(19) Nielsen, S. O.; Michael, B. D.; Hart, E. J. *J. Phys. Chem.* **1976**, *80*, 2482.

(20) Tauber, M. J.; Mathies, R. A. *Chem. Phys. Lett.* **2002**, *354*, 518; *J. Phys. Chem. A* **2001**, *105*, 10952; *J. Am. Chem. Soc.* **2003**, *125*, 1394.

(21) Mizuno, M.; Tahara, T. *J. Phys. Chem. A* **2001**, *105*, 8823; **2003**, *107*, 2411. Mizuno, M.; Yamaguchi, S.; Tahara, T. In *Femtochemistry and Femtobiology*; Martin, M. M., Hynes, J. T., Eds.; Elsevier: Amsterdam, The Netherlands, 2004; p 225.

(22) Verlet, L. *Phys. Rev.* **1967**, *159*, 98.

(23) Berendsen, H. J. C.; Postma, J. P.; van Gunsteren, W. F.; Hermans, J. *Intermolecular Forces*; Reidel: Dordrecht, The Netherlands, 1981. Reimers, J. R.; Watts, R. O. *Mol. Phys.* **1984**, *52*, 357. Toukan, K.; Rahman, A. *Phys. Rev. B: Condens. Matter Mater. Phys.* **1985**, *31*, 2643.

(24) Rossky, P. J.; Schnitker, J. *J. Phys. Chem.* **1988**, *92*, 4277.

(25) Cullum, J. K.; Willoughby, R. A. *Lanczos Algorithms for Large Symmetric Eigenvalue Computations*, Birkhauser, Boston, MA, 1985. See also: Webster, F.; Rossky, P. J.; Friesner, R. A. *Comp. Phys. Comm*. **1991**, *63*, 494.

(26) Bradforth, S. E.; Jungwirth, P. *J. Phys. Chem. A* **2002**, *106*, 1286.

(27) Cabral do Couto, P.; Estacio, S. G.; Costa Cabral, B. J. *J. Chem. Phys.* **2005**, *123*, 054510.

(28) Becke, A. D. *Phys. Rev. A: At., Mol., Opt. Phys.* **1988**, *38*, 3098.

(29) Lee, C.; Yang, W.; Parr, R. G. *Phys. Rev. B: Condens. Matter Mater. Phys.* **1988**, *37*, 785.

(30) Frisch, M. J.; Trucks, G. W.; Schlegel, H. B.; Scuseria, G. E.; Robb, M. A.; Cheeseman, J. R.; Zakrzewski, V. G.; Montgomery, J. A., Jr.; Stratmann, R. E.; Burant, J. C.; Dapprich, S.; Millam, J. M.; Daniels, A. D.; Kudin, K. N.; Strain, M. C.; Farkas, O.; Tomasi, J.; Barone, V.; Cossi, M.; Cammi, R.; Mennucci, B.; Pomelli, C.; Adamo, C.; Clifford, S.; Ochterski, J.; Petersson, G. A.; Ayala, P. Y.; Cui, Q.; Morokuma, K.; Malick, D. K.; Rabuck, A. D.; Raghavachari, K.; Foresman, J. B.; Cioslowski, J.; Ortiz, J. V.; Stefanov, B. B.; Liu, G.; Liashenko, A.; Piskorz, P.; Komaromi, I.; Gomperts, R.; Martin, R. L.; Fox, D. J.; Keith, T.; Al-Laham, M. A.; Peng, C. Y.; Nanayakkara, A.; Gonzalez, C.; Challacombe, M.; Gill, P. M. W.; Johnson, B. G.; Chen, W.; Wong, M. W.; Andres, J. L.; Head-Gordon, M.; Replogle, E. S.; Pople, J. A. *Gaussian 98, revision A.1*, Gaussian, Inc., Pittsburgh, Pennsylvania, 1998.

(31) Hermosilla, L.; Calle, P.; de la Vega, J. M. G.; Sieiro, C. *J. Phys. Chem. A* **2005**, 109, *1114*

(32) Atkins, P. W.; Symons, M. C. R. *The Structure of Inorganic Radicals*; Elsevier: Amsterdam, 1967.

(33) Bartels, D. M. *J. Chem. Phys.* **2001**, *115*, 4404. Tuttle, T. R., Jr.; Golden, S. *J. Phys. Chem.* **1991**, *95*, 5725.

(34) Jou, F.-Y.; Freeman, G. R. *J. Phys. Chem.* **1979**, *83*, 2383.

(35) Shkrob, I. A. *J. Phys. Chem. A* **2006**, *110*, 3967.

(36) Winter, B.; Faubel, M. *Chem. Rev. 2006*, **106**, 1176.

(37) Lee, H. M.; Suh, S. B.; Tarakeshwar, P.; Kim, K. S. *J. Chem. Phys.* **2005**, *122*, 044309.

(38) Ermoshin, V. A.; Sobolewski, A. L.; Domcke, W. *Chem. Phys. Lett.* **2002**, *356*, 556. Sobolewski, A. L.; Domcke, W. *J. Phys. Chem. A* **2002**, *106*, 4158; *Phys. Chem. Chem. Phys.* **2003**, *5*, 1130. Neumann, S.; Eisfeld, W.; Sobolewski, A. L., Domcke, W. *Phys. Chem. Chem. Phys.* **2004**, *6*, 5297

(39) Herbert, J. M.; Head-Gordon, M. *J. Am. Chem. Soc.* **2006**, *128*, 13293.

(40) Copeland, D. A.; Kesner, N. R.; Jortner, J. *J. Chem. Phys.* **1970**, *53*, 1189.

(41) Symons, M. C. R. *Chem. Soc. Rev.* **1976**, *5*, 337.